

3D modeling of positive streamers in air with inhomogeneous density

Baohong Guo¹ , Ute Ebert^{1,2}  and Jannis Teunissen^{1,*} 

¹ Centrum Wiskunde & Informatica (CWI), Amsterdam, The Netherlands

² Department of Applied Physics, Eindhoven University of Technology, Eindhoven, The Netherlands

E-mail: jannis.teunissen@cw.nl

Received 12 May 2023, revised 22 August 2023

Accepted for publication 11 September 2023

Published 25 September 2023



Abstract

We study the effect of an inhomogeneous gas density on positive streamer discharges in air using a 3D fluid model with stochastic photoionization, generalizing earlier work with a 2D axisymmetric model by Starikovskiy and Aleksandrov (2019 *Plasma Sources Sci. Technol.* **28** 095022). We consider various types of planar and (hemi)spherical gas density gradients. Streamers propagate from a region of density n_0 towards a region of higher or lower gas density n_1 , where n_0 corresponds to 300 K and 1 bar. We observe that streamers can always propagate into a region with a lower gas density. When streamers enter a region with a higher gas density, branching can occur at the density gradient, with branches growing in a flower-like pattern over the gradient surface. Depending on the gas density ratio, the gradient width and other factors, narrow branches are able to propagate into the higher-density gas. In a planar geometry, we find that such propagation is possible up to a gas density slope of $3.5 n_0/\text{mm}$, although this value depends on a number of conditions, such as the gradient angle. Surprisingly, a higher applied voltage makes it more difficult for streamers to penetrate into the high-density region, due to an increase of the primary streamer's radius.

Keywords: 3D modeling, streamer discharge, branching, inhomogeneous gas, gas density

(Some figures may appear in colour only in the online journal)

1. Introduction

Streamer discharges are an initial phase of electric breakdown when an insulating medium is subjected to a high applied voltage [1]. They feature thin plasma channels which largely screen the electric field in their interiors, leading to field enhancement at their tips where they grow due to electron impact ionization. Streamers are precursors of sparks and lightning leaders [2, 3], and they occur in the upper atmosphere above thunderclouds as sprites [4], as well as in high-voltage technology [5, 6]. Due to their highly non-equilibrium nature, streamers are also widely used for many plasma applications [7, 8].

1.1. Streamer dynamics in varying gas densities

Streamers can occur at various pressures and in different gases [9]. Streamer dynamics change in different gas densities according to scaling laws [10, 11]: all length and time scales of a streamer scale with the inverse gas density $1/n$, the electric field scales as $E \sim n$, and the electron density scales as $n_e \sim n^2$.

Streamer propagation in inhomogeneous gas media, where the gas composition or density varies spatially, can be observed under natural and industrial conditions. This phenomenon has recently been investigated in air by Starikovskiy *et al* using a 2D axisymmetric fluid model [12–14]. In [12], the calculations showed how the streamer dynamics changed when a positive streamer developed through a shock wave from a high-density to a low-density region where the air density changed sharply, in agreement with their experimental observations in shock-tube experiments [12]. In [13], the authors further computationally studied the interaction of

* Author to whom any correspondence should be addressed.

streamers with varying air density discontinuities, focusing on the opposite case when a positive streamer propagated from a low-density to a high-density region. They found a streamer was unable to penetrate into the high-density region when the density ratio between two different regions was sufficiently large. Instead, the streamer was observed to develop along the surface between the two regions. This phenomenon was summarized by the authors as ‘*a gas density discontinuity forms a kind of ‘gas-dynamic diode’ that allows the plasma channel to propagate in one direction and blocks its development in another*’ [13]. The authors also performed simulations of streamers interacting with gaseous layers of varying densities at both polarities [14]. They found that negative streamers could pass through a thin low-density layer whereas positive ones could not.

The simulations discussed above were all performed assuming axisymmetric symmetry. The goal of this paper is to computationally study these phenomena in a full 3D geometry. This makes it possible to study the effects of streamer branching, which will be shown to be an important mechanism when streamers interact with gas density gradients. Furthermore, we consider more general gas density gradients than in previous work.

1.2. Gas density inhomogeneities

Gas density inhomogeneities can be induced by shock waves and heating processes. An early simulation conducted by Marode *et al* [15] showed that discharge channels could heat air and initiate a radial flow of neutral air molecules, reducing the air density in the path by up to 50%. Such air perturbations have been further studied computationally in [16–18], and measured experimentally in [18–25]. These studies confirm the presence of spherical or plane shock waves and gas thermal expansion in association with spark and leader discharges. Such phenomena can heat air to temperatures exceeding thousands of Kelvin and result in a significant decrease in air density. Furthermore, Köhn *et al* computationally investigated how sinusoidal air density perturbations induced by discharge shock waves affected streamer properties and the generation of runaway electrons [26–28].

Density perturbations can also be observed around high-speed aircraft or in strong airflows [29–33]. In plasma aerodynamics, streamer discharges such as nanosecond surface dielectric barrier discharges can be used to control airflow perturbations generated by shock waves, rarefaction waves and jet injection [34–38].

Other ways to create gas density inhomogeneities can be the presence of fuel vapor and fuel aerosols or flame in fuel-air mixtures used in plasma-assisted combustion. In [39], experiments were performed in a counterflow non-premixed flame environment, and the results showed that nanosecond pulsed discharges were localized in the area around the front of the counter-flow flame due to a significant decrease in gas density formed by gas heating.

Finally, in Earth’s atmosphere the air density varies with altitude, with a scale height of about 8 km. This variation affects discharges in the upper atmosphere, in particular so-called sprites, which are essentially streamer discharges. The effects of gas density on sprites were numerically studied in [40–42], and experimentally measured (on a much smaller scale) using a hot jet which led to a density ratio of two [43].

2. 3D fluid model

We simulate positive streamers in dry air consisting of 80% N₂ and 20% O₂ at 300 K with two regions of different air densities connected by a density gradient, see section 2.4. Simulations are performed with a 3D drift-diffusion-reaction type fluid model with the local field approximation, using the open-source Afivo-streamer code [44].

2.1. Model equations

The electron density n_e evolves in time as

$$\partial_t n_e = \nabla \cdot (\mu_e \mathbf{E} n_e + D_e \nabla n_e) + S_e + S_{ph}, \quad (1)$$

where μ_e is the electron mobility, D_e the electron diffusion coefficient, \mathbf{E} the electric field. S_e is an electron source term due to reactions involving electrons, see table 1. S_{ph} is a non-local photoionization source term described by Zheleznyak’s model [45]. This model can be solved by either a continuum (Helmholtz approximation) approach or a stochastic (Monte Carlo) method [46–48], see [49] for a comparison. We here use stochastic photoionization with discrete ionizing photons using the same parameters as [50], which were shown to reproduce streamer branching as observed in experiments [50]. For simplicity, we do not take the variation of the photon absorption length with the gas density into account. The effects of this approximation will be discussed in section 5.3.

All species other than electrons are assumed to be immobile, and we do not consider gas dynamics. Species densities evolve according to reactions listed in table 1. The electric field \mathbf{E} is calculated as $\mathbf{E} = -\nabla \phi$. The electric potential ϕ is obtained by solving Poisson’s equation

$$\nabla^2 \phi = -\rho / \epsilon_0, \quad (2)$$

where ρ is the space charge density and ϵ_0 is the vacuum permittivity. Equation (2) is solved using the geometric multigrid method included in the Afivo library [51, 52].

2.2. Reaction set and input data

Since we consider short time scales (up to tens of nanoseconds), we use a relatively small set of chemical reactions, which includes the main reactions between electrons, ions, and neutrals, as shown in table 1.

Electron transport coefficients μ_e and D_e in equation (1), and reaction rate coefficients ($k_1 - k_9$) in table 1, are functions

Table 1. List of reactions included in the model, with reaction rate coefficients and references. The symbol M denotes a neutral molecule (either N₂ or O₂). The reduced electric field E/n is in units of Td (Townsend). $T(K)$ and $T_e(K) = 2\epsilon_e/3k_B$ are gas and electron temperatures, respectively, where k_B is the Boltzmann constant and ϵ_e is the mean electron energy computed with BOLSIG+ [53].

No.	Reaction	Reaction rate coefficient	Reference
R1	$e + N_2 \rightarrow e + e + N_2^+$ (15.60 eV)	$k_1(E/n)$	[54, 55]
R2	$e + N_2 \rightarrow e + e + N_2^+$ (18.80 eV)	$k_2(E/n)$	[54, 55]
R3	$e + O_2 \rightarrow e + e + O_2^+$ (12.06 eV)	$k_3(E/n)$	[54, 56]
R4	$e + O_2 + O_2 \rightarrow O_2^- + O_2$	$k_4(E/n)$	[54, 56]
R5	$e + O_2 \rightarrow O^- + O$	$k_5(E/n)$	[54, 56]
R6	$O_2^- + M \rightarrow e + O_2 + M$	$1.24 \times 10^{-11} \exp(-(\frac{179}{8.8+E/n})^2) \text{ cm}^3 \text{ s}^{-1}$	[57]
R7	$O^- + N_2 \rightarrow e + N_2O$	$1.16 \times 10^{-12} \exp(-(\frac{48.9}{11+E/n})^2) \text{ cm}^3 \text{ s}^{-1}$	[57]
R8	$O^- + O_2 + M \rightarrow O_3^- + M$	$1.10 \times 10^{-30} \exp(-(\frac{E/n}{65})^2) \text{ cm}^6 \text{ s}^{-1}$	[57]
R9	$O^- + O_2 \rightarrow O_2^- + O$	$6.96 \times 10^{-11} \exp(-(\frac{198}{5.6+E/n})^2) \text{ cm}^3 \text{ s}^{-1}$	[57]
R10	$N_2^+ + O_2 \rightarrow O_2^+ + N_2$	$6.00 \times 10^{-11} (\frac{300}{T})^{0.5} \text{ cm}^3 \text{ s}^{-1}$	[58]
R11	$N_2^+ + N_2 + M \rightarrow N_4^+ + M$	$5.00 \times 10^{-29} (\frac{300}{T})^2 \text{ cm}^6 \text{ s}^{-1}$	[58, 59]
R12	$N_4^+ + O_2 \rightarrow O_2^+ + N_2 + N_2$	$2.50 \times 10^{-10} \text{ cm}^3 \text{ s}^{-1}$	[58]
R13	$O_2^+ + O_2 + M \rightarrow O_4^+ + M$	$2.40 \times 10^{-30} (\frac{300}{T})^3 \text{ cm}^6 \text{ s}^{-1}$	[58, 59]
R14	$e + N_4^+ \rightarrow N_2 + N_2$	$2.00 \times 10^{-6} (\frac{300}{T_e})^{0.5} \text{ cm}^3 \text{ s}^{-1}$	[58]
R15	$e + O_4^+ \rightarrow O_2 + O_2$	$1.40 \times 10^{-6} (\frac{300}{T_e})^{0.5} \text{ cm}^3 \text{ s}^{-1}$	[58]

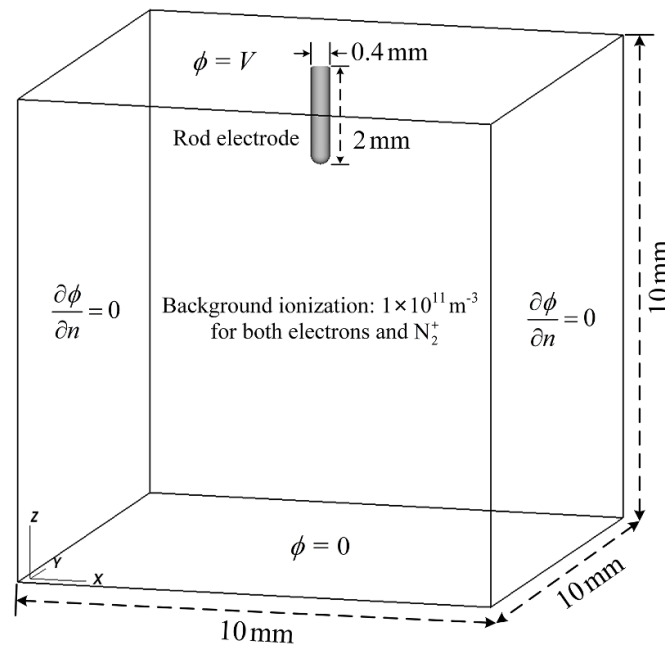


Figure 1. A view of the $(10 \text{ mm})^3$ computational domain. The rod electrode protruding from the upper plate from which a streamer starts has a length of 2 mm and a diameter of 0.4 mm. Boundary conditions for the electric potential ϕ are indicated.

of n and of the reduced electric field E/n , where E is the electric field and n is the gas number density. These coefficients were computed with BOLSIG+ [53], with electron-neutral cross sections for N₂ and O₂ obtained from the Phelps database [54–56].

2.3. Computational domain and initial condition

We use a cubic computational domain that measures $(10 \text{ mm})^3$, as illustrated in figure 1. The domain has a plate-plate geometry with a centrally positioned electrode protruding from

the upper plate. The electrode is rod-shaped with a semi-spherical tip, with a length of 2 mm and a diameter of 0.4 mm.

For all species densities, homogeneous Neumann boundary conditions are applied on all domain boundaries, including the rod electrode. For the electric potential, homogeneous Neumann boundary conditions are applied on the sides of the domain. The lower plate is grounded, and a constant high voltage V is applied on the upper plate and the rod electrode. The applied voltage V is always 16 kV, except for the cases in section 3.1.4 where it is varied between 12 kV and 18 kV to investigate its influence on streamer interaction with air density gradients. In the simulations, the reduced background

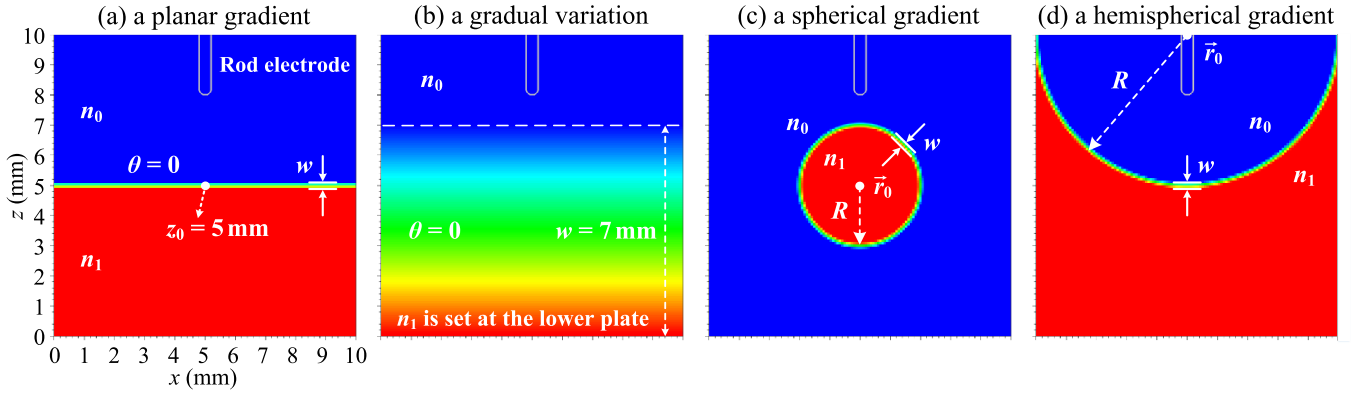


Figure 2. x - z view of four types of air density gradients. The blue and red regions denote the gas number density as n_0 and n_1 , respectively. The air density changes linearly in space between these two regions over a width w . Panel (a) shows a planar gradient indicating its center height as z_0 and its angle with respect to the x - y plane as θ . Panel (b) shows a gradual variation with $w = 7$ mm and $\theta = 0$. Panels (c) and (d) show a spherical and a hemispherical gradient, respectively, where the gradient center is marked as \vec{r}_0 with a radius R .

Table 2. Summary of four types of air density gradients used in the present paper, corresponding to figure 2.

Gradient type	Planar	Gradual	Spherical	Hemispherical
Applied voltages	12–18 kV	16 kV	16 kV	16 kV
Constant parameters	—	$w = 7$ mm, $\theta = 0$	$w = 0.2$ mm, $R = 2$ mm	$w = 0.2$ mm, $R = 5$ mm, $\vec{r}_0 = (5 \text{ mm}, 5 \text{ mm}, 10 \text{ mm})$
Variable parameters	n_1, θ, w, z_0	n_1	n_1, \vec{r}_0	n_1
Simulation results	sections 3 and 5.1	section 4.3	section 4.1	section 4.2

electric field always remains below the reduced breakdown electric field (where the impact ionization rate is equal to the attachment rate).

As an initial condition, homogeneous background ionization with a density of 10^{11} m^{-3} for both electrons and N_2^+ is included for discharge inception. After inception photoionization will quickly become the dominant source of free electrons for sustaining streamer propagation in air [60]. All other ion densities are initially zero.

For computational efficiency, the Afivo-streamer code includes adaptive mesh refinement. We apply the same refinement criteria to determine the grid spacing Δx as [61], and the minimal grid spacing is $1.22 \mu\text{m}$ in the simulations.

2.4. Air density gradients

Four types of air density gradients are used, with an example of each illustrated in figure 2. Two regions can be identified with different gas number densities, denoted as n_0 and n_1 , respectively. Here n_0 , located in the region near the rod electrode, is always $2.414 \times 10^{25} \text{ m}^{-3}$ (the air density at 1 bar and 300 K), whereas n_1 is varied. For simplicity, we here assume that the temperature is also 300 K in the region n_1 . Note that in reality, air density differences are due to a combination of temperature and pressure variations, with temperature variations typically persisting longer. In the simulations, the air density n affects all parameters related to both the density itself and the reduced

electric field E/n , including reaction rate coefficients ($k_1 - k_9$) in table 1 and electron transport coefficients μ_e and D_e .

The air density changes linearly in space between n_0 and n_1 over a spatial width w . For a planar density gradient shown in figure 2(a), the center height of the gradient is indicated as z_0 and the angle of the gradient with respect to the x - y plane is marked as θ . The gradual density variation shown in figure 2(b) is basically similar to figure 2(a), with a much wider gradient of $w = 7$ mm until the bottom plate. The spherical and hemispherical density gradients shown in figures 2(c) and (d) are characterized by the gradient center \vec{r}_0 with a radius R . For details on how these gas density variations were implemented in the code, see appendix. The simulation parameters used in the present paper are summarized in table 2.

The time step is restricted according to several criteria as given in [51, 62]. Simulations are stopped when the time step becomes smaller than 10^{-14} s or when the discharge reaches the lower plate. A small time step can occur when a narrow branch forms with a very high electron density and a high electric field, see e.g. figure 3, which leads to a small dielectric relaxation time.

3. Interaction with planar density gradients

In this section, we investigate the interaction between a positive streamer and a planar density gradient, see figure 2(a) and table 2. Both the case where a streamer propagates from a low-density region to a high-density region ($n_1 > n_0$) and the

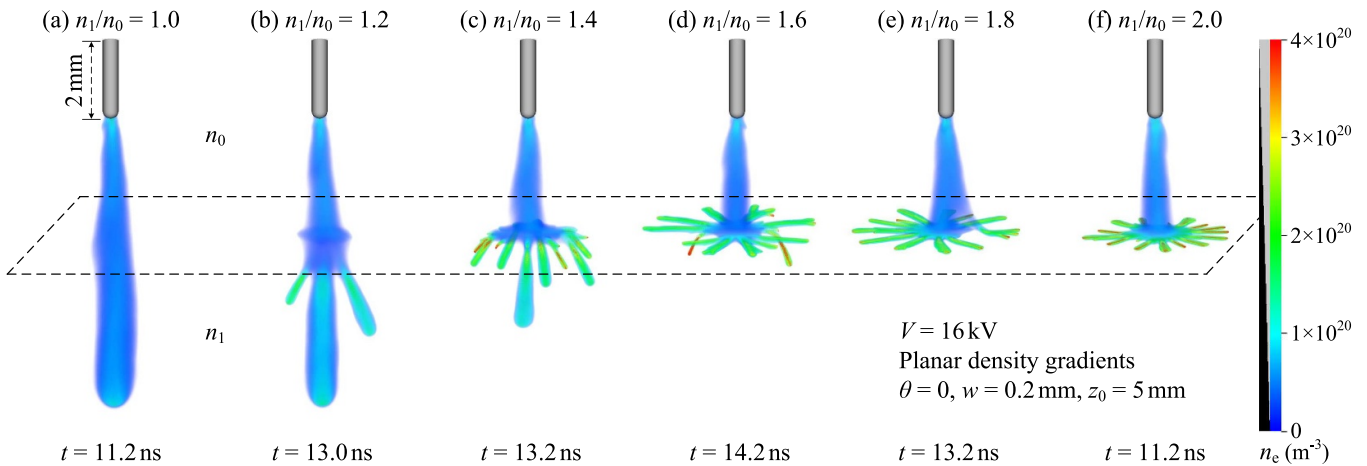


Figure 3. The interaction between a positive streamer in air and a planar density gradient in a 3D simulation as the streamer propagates from a low-density region to a high-density region. Streamers for different density ratios n_1/n_0 at an applied voltage $V = 16$ kV are shown at the last time moment. The planar gradient is indicated by a dashed box. Shown is a 3D volume rendering of the electron density n_e with a linear scale ranging from 0 to $4 \times 10^{20} \text{ m}^{-3}$ through Visit [63]; the opacity is indicated in the legend. The same visualization is applied to all subsequent figures presented in the paper.

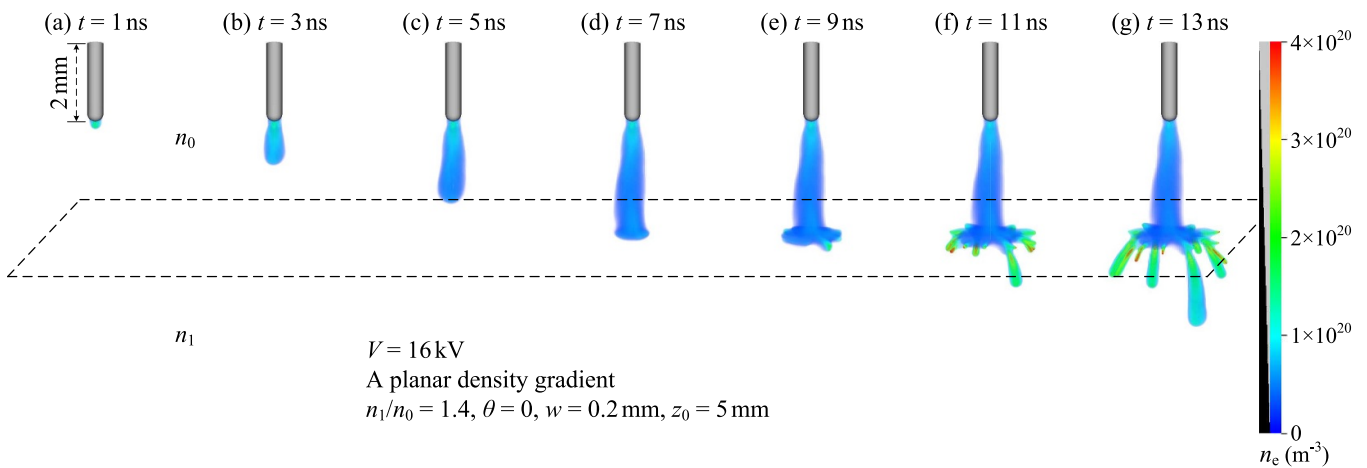


Figure 4. Time evolution of the electron density n_e for figure 3(c) with $n_1/n_0 = 1.4$ in time steps of 2 ns.

opposite case ($n_1 < n_0$) are considered, for which 3D simulation results are presented in sections 3.1 and 3.2, respectively. In the simulations we vary the center height z_0 of the gradient, the gradient angle θ (with respect to the x - y plane), the gradient width w and the applied voltage V from their default values of $z_0 = 5$ mm, $\theta = 0$, $w = 0.2$ mm and $V = 16$ kV. The air density ratio n_1/n_0 is also varied.

3.1. From a low-density to a high-density region

3.1.1. Effect of the air density ratio n_1/n_0 . Figure 3(a) shows that a non-branching single streamer is visible in the absence of a density gradient ($n_1/n_0 = 1.0$). As the density ratio increases to $n_1/n_0 = 1.2$, the planar gradient starts to slightly affect streamer propagation, but the streamer can still penetrate into the high-density region with two extra branches, see figure 3(b). When n_1/n_0 further increases to 1.4–1.6, multiple branching channels propagate along the surface of the planar

gradient, see figures 3(c) and (d). The discharge can still enter the high-density region after propagating a certain distance on the surface, which will be further discussed later. Finally, the streamer is inhibited from propagating through the gradient (up to the time scales considered) when the density ratio is sufficiently high (e.g. $n_1/n_0 \geq 1.8$), see figures 3(e) and (f). In this case, the streamer propagates along the gradient surface relatively slowly (at a velocity of about 0.2 – $0.3 \times 10^6 \text{ m s}^{-1}$) since there is no parallel component of the background electric field along the gradient surface. The discharge forms a flower-like structure, which is similar to the propagation along a dielectric surface in a barrier discharge. There are high electric fields at the tips of the branched channels, and the electron density in some channels exceeds 10^{21} m^{-3} (which is well above the limit of the color scale).

The time evolution of the streamer with $n_1/n_0 = 1.4$ in figure 3(c) is shown in figure 4. The streamer initiates from the rod electrode tip and then propagates downwards at a velocity

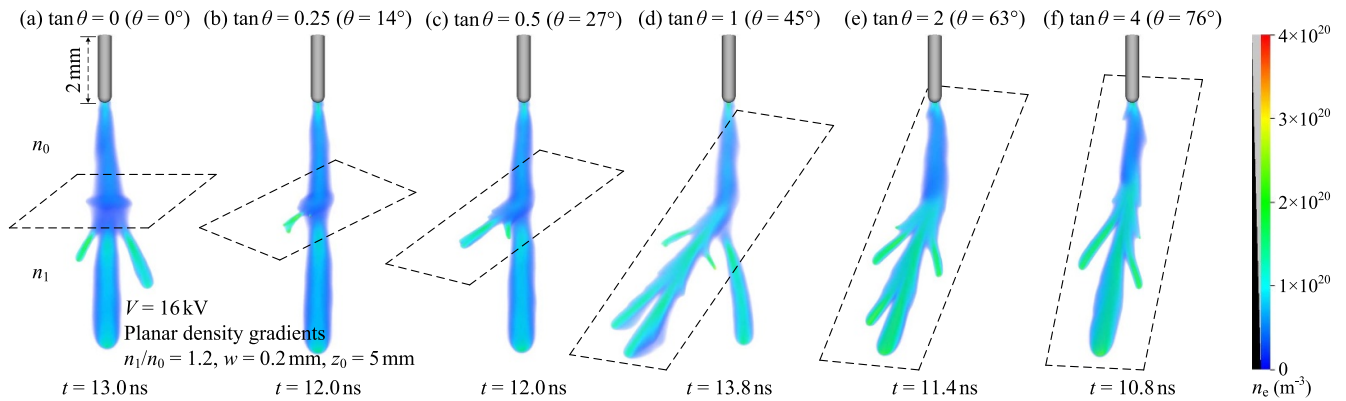


Figure 5. Effect of the gradient angle θ on streamer propagation for figure 3(b) with $n_1/n_0 = 1.2$. The planar gradient is indicated by a dashed box in all panels. An increase in θ facilitates streamer propagation along the gradient surface.

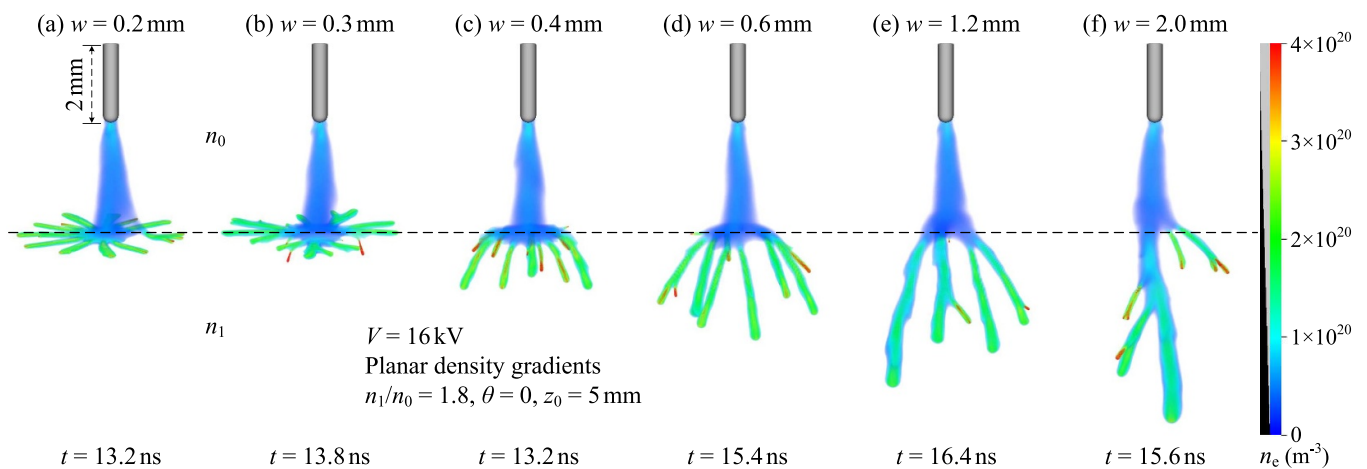


Figure 6. Effect of the gradient width w on streamer propagation for figure 3(e) with $n_1/n_0 = 1.8$. The planar gradient is here and afterward indicated by a dashed line. An increase in w allows the streamer to overcome the gradient.

of about $0.5 \times 10^6 \text{ m s}^{-1}$, and the streamer radius expands with time until approaching the planar gradient. When the streamer interacts with the gradient, it is slowed down and inhibited from propagating through the gradient. Instead, the streamer propagates along the gradient surface at a velocity of about $0.2 \times 10^6 \text{ m s}^{-1}$ and splits into several branches, leading to decreased radii and increased electric fields at the streamer heads. Subsequently, this allows the branching channels to eventually enter the high-density region and continue their downward propagation at a velocity of about $0.4 \times 10^6 \text{ m s}^{-1}$. In this region, the streamer channels have smaller radii, higher electric fields, and higher electron densities, as could be expected from the scaling laws mentioned in the introduction.

3.1.2. Effect of the gradient angle θ . The effect of the gradient angle θ is illustrated in figure 5. For $\theta = 0$ with $n_1/n_0 = 1.2$, the streamer shown in figure 5(a) can propagate through the planar gradient. Increasing θ causes the streamer to split into two parts when it encounters the gradient, where the first part penetrates into the high-density region in the original

direction, and the second part propagates along the gradient surface, see figures 5(b) and (c). As θ further increases to about $\tan\theta = 1$ shown in figure 5(d), the surface component becomes dominant, forming several side branches. When θ becomes even higher (e.g. $\tan\theta \geq 2$) the streamer only propagates along the gradient surface, see figures 5(e) and (f). In conclusion, increasing the gradient angle θ facilitates streamer propagation along the gradient surface due to the increased component of the background electric field along the surface.

3.1.3. Effect of the gradient width w . Figure 6 illustrates the effect of the gradient width w . For $w = 0.2 \text{ mm}$ with $n_1/n_0 = 1.8$ and $\theta = 0$, the streamer is inhibited from propagating through the gradient and it forms a flower-like structure, see figure 6(a). However, this inhibition can be overcome by increasing the gradient width. When w increases to 0.3 mm shown in figure 6(b), most of the branching channels still propagate along the gradient surface, whereas the rest of them enter the high-density region with much higher electron

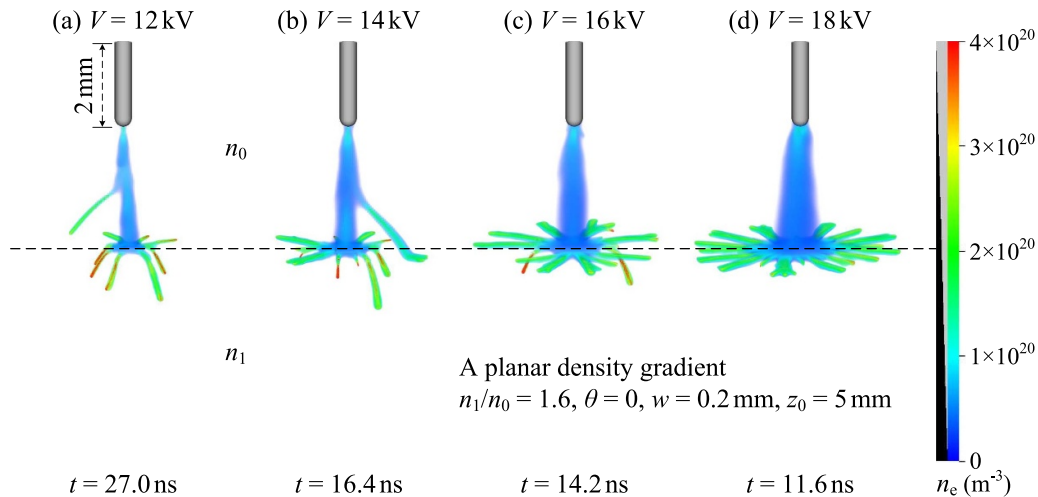


Figure 7. Effect of the applied voltage V on streamer propagation for figure 3(d) with $n_1/n_0 = 1.6$. Surprisingly, the streamer more easily propagates through the gradient with a lower applied voltage.

densities inside the thin branching channels. For w exceeding 0.4 mm, all streamer branches can eventually penetrate into the high-density region, with fewer branching channels being formed for larger w , see figures 6(c)–(f). Note that Starikovskiy and Aleksandrov observed a similar effect that allowed the streamer to propagate through the gradient by increasing the gradient width in [13], which occurred when the gradient width became comparable to the streamer radius. Here we find that this effect also depends on the density slope, which will be further elaborated in section 5.1.

3.1.4. Effect of the applied voltage V . The effect of the applied voltage V is illustrated in figure 7. For $V = 12$ kV with $n_1/n_0 = 1.6$, $\theta = 0$ and $w = 0.2$ mm, the streamer can propagate through the gradient and form several branching channels, see figure 7(a). As V increases to 14–16 kV, the radius of the streamer in the low-density region also increases. This makes it more difficult for the streamer to enter the high-density region, resulting in the formation of more branching channels along the surface, see figures 7(b) and (c). When V further increases to 18 kV, the streamer is inhibited from propagating through the gradient, see figure 7(d). Note that the interaction between a positive streamer and a planar gradient resembles the behavior of archery, where an arrow with a sharper tip is more likely to pierce the target. In addition, the streamer in the low-density region is more prone to branch at lower applied voltages.

In [13] it was argued that the ability of a streamer to propagate through a sharp density discontinuity increased with the applied voltage due to an increase in the reduced background electric field E/n . However, in figure 7 we observe the opposite effect: a streamer more easily propagates through a planar gradient with a lower applied voltage. Whether a streamer can propagate through such a gradient depends on many factors, including e.g. the streamer radius, the background electric field and the gradient angle. For the cases considered here the main

factor appears to be the streamer radius, with a larger radius making it more likely for the streamer to deform into a ‘surface’ discharge.

In figure 8 we vary the center height z_0 of the gradient, with other parameters the same as in figure 7(d). As expected, reducing the distance between the electrode tip and the gradient results in a smaller streamer radius and an increased background field at the gradient, thereby collectively facilitating the propagation of the streamer into the high-density region.

3.2. From a high-density to a low-density region

Figure 9 shows the effects of the air density ratio n_1/n_0 and the gradient angle θ on streamer propagation. As expected, for $n_1/n_0 < 1$ with $\theta = 0$ the streamer can propagate through the planar gradient, forming a small discontinuity at the gradient, see figure 9(a). This discontinuity of streamer propagation is attributed to the change in the reduced background electric field E/n caused by the air density gradient. In the low-density region the streamer radius increases, whereas the electric field at the streamer head and the electron density in the streamer channel decrease compared to the high-density region.

The effect of the gradient angle θ is illustrated in figure 9(b). For $\theta > 0$ with $n_1/n_0 = 0.7$, the streamer deviates from its original path after it encounters the gradient. More specifically, the streamer propagates perpendicular to the gradient upon encountering it, and continues its propagation along the background electric field in the low-density region. This deviation becomes more prominent as θ increases. In addition to the primary channel, another branching channel initiated by the lower tip of the streamer when encountering the gradient is observed to continue propagating in the high-density region when θ increases to $\tan\theta = 4$. Note that this branching channel is repelled from the gradient surface by the primary channel.

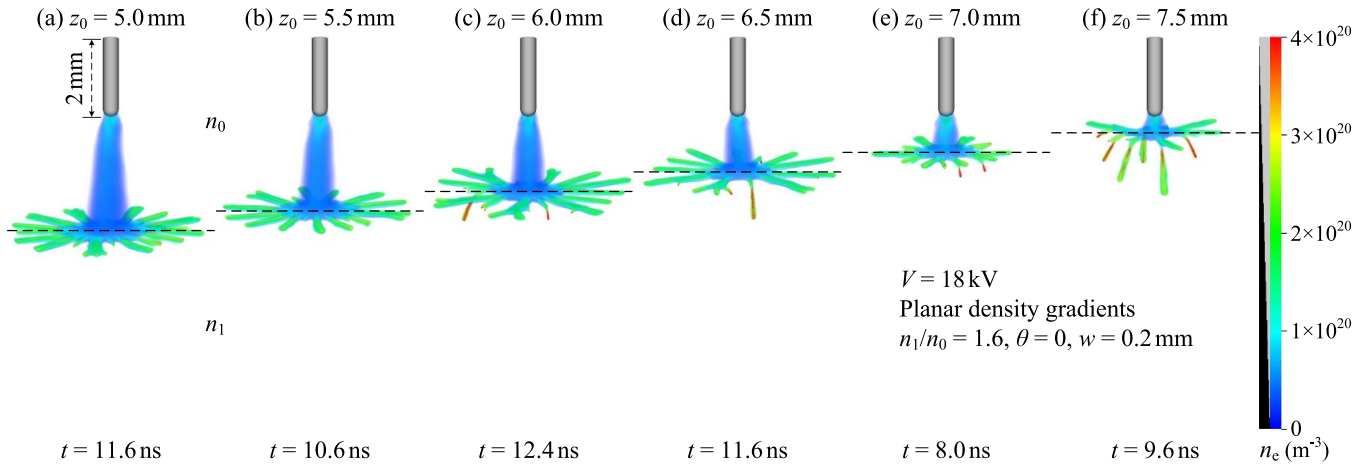


Figure 8. Effect of the distance between the electrode tip and the gradient on streamer propagation. The center height z_0 of the gradient is varied, and other parameters are the same as in figure 7(d). When the gradient is close to the electrode ($z_0 \geq 6.0$ mm), the streamer can propagate into the high-density region.

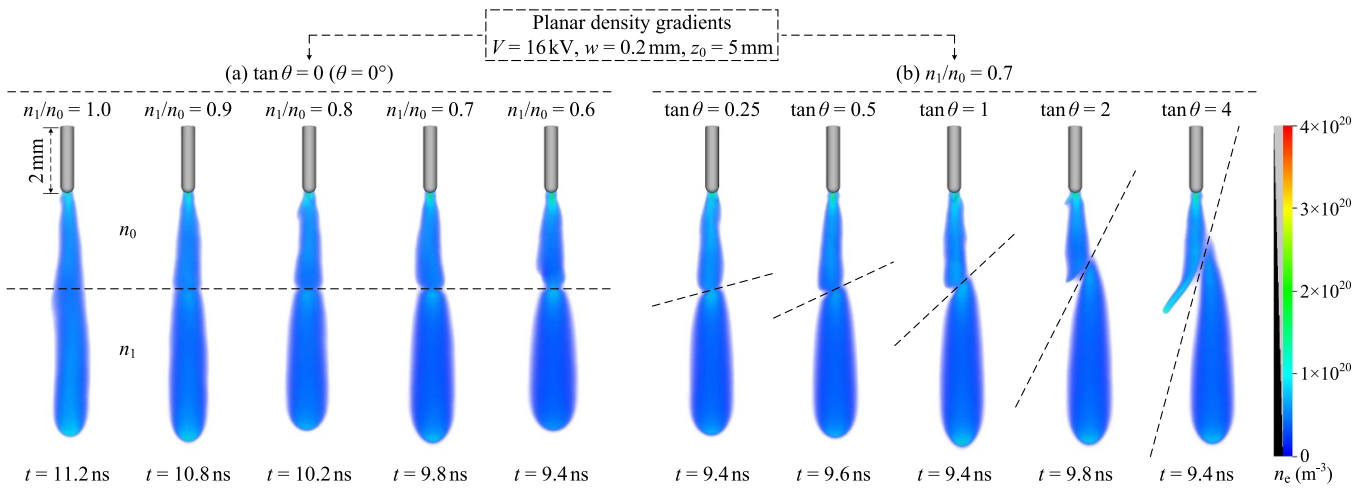


Figure 9. Streamer propagation from a high-density region to a low-density region. Panel (a) shows streamers for different density ratios n_1/n_0 at an angle $\theta = 0$, whereas panel (b) shows streamers for different gradient angles θ at a density ratio $n_1/n_0 = 0.7$.

4. Interaction with non-planar gradients

4.1. Spherical density gradient

We first investigate how a positive streamer interacts with a spherical density gradient, see figure 2(c) and table 2. Similar to section 3, we consider both cases where $n_1 > n_0$ and $n_1 < n_0$. In the simulations, the air density ratio n_1/n_0 and the gradient center \vec{r}_0 are varied, whereas the sphere radius $R = 2$ mm, the gradient width $w = 0.2$ mm and the applied voltage $V = 16$ kV are kept constant.

Figure 10 shows the case $n_1/n_0 > 1$. For $n_1/n_0 = 1.2$ with $\vec{r}_0 = (5 \text{ mm}, 5 \text{ mm}, 5 \text{ mm})$, the streamer can propagate through the gradient and enter its interior with multiple irregular branches, see figure 10(a). When the density ratio increases to $n_1/n_0 \geq 1.4$, the streamer is inhibited from propagating through the gradient. Instead, it propagates along the spherical surface with several branching channels. After approaching the same height as the sphere's center, the branching channels

propagate vertically downwards along the background electric field. Note that the initial interaction of a streamer with a spherical gradient is similar to that with a planar gradient at the same angle, but that the subsequent propagation depends on the gradient's curvature.

Furthermore, when the spherical gradient is horizontally moved to the right for $n_1/n_0 = 1.4$, as shown in figure 10(b), the streamers only interact with the left side of the sphere and propagate along its surface.

Figure 11 shows that when $n_1/n_0 < 1$ the streamers can propagate through the top and bottom of the gradient and form small discontinuities at the gradient. For $n_1/n_0 = 0.7$ in figure 11(b), when the spherical gradient is horizontally moved off-center at $\vec{r}_0 = (7 \text{ mm}, 5 \text{ mm}, 5 \text{ mm})$, a branching channel is visible outside the sphere, similar to figure 9(b) for the case $\tan \theta = 4$. Inside the sphere, the discharge splits into two parts upon encountering the bottom of the gradient, where the first part propagates through the gradient and continues propagating in the high-density region, and the second part propagates

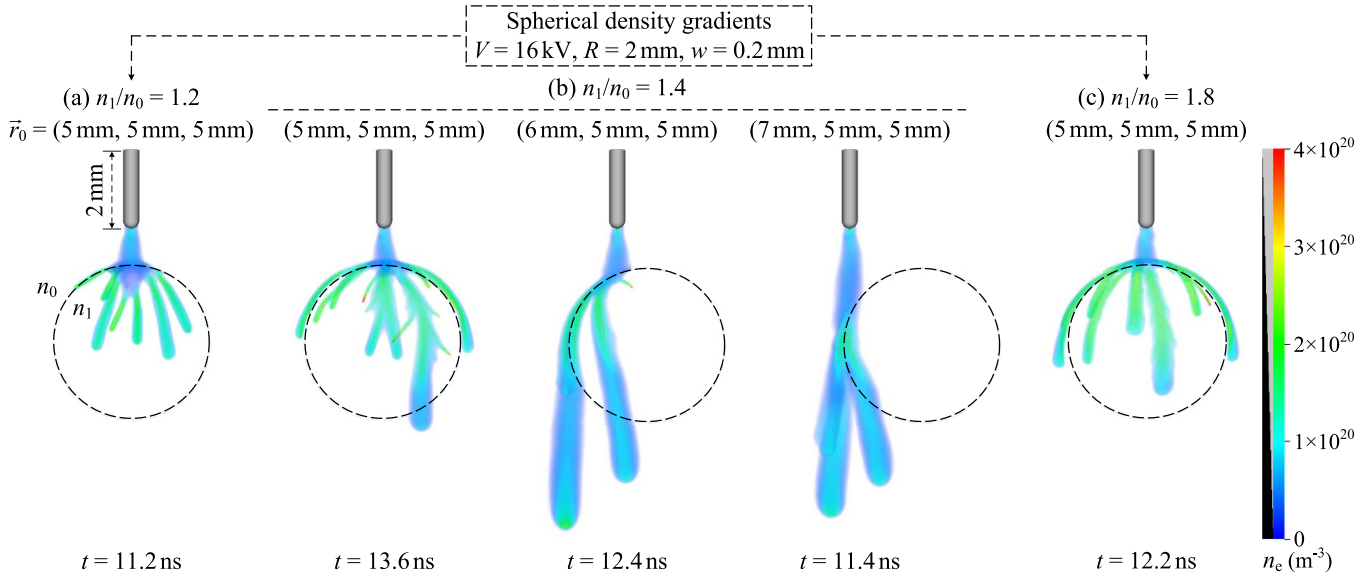


Figure 10. The interaction between a streamer and a spherical density gradient for $n_1/n_0 > 1$. Panels (a) and (c) show streamers for different density ratios n_1/n_0 at a gradient center $\vec{r}_0 = (5 \text{ mm}, 5 \text{ mm}, 5 \text{ mm})$, whereas panel (b) shows streamers for different gradient centers \vec{r}_0 at a density ratio $n_1/n_0 = 1.4$. The spherical gradient is here and afterward indicated by a dashed circle in all panels.

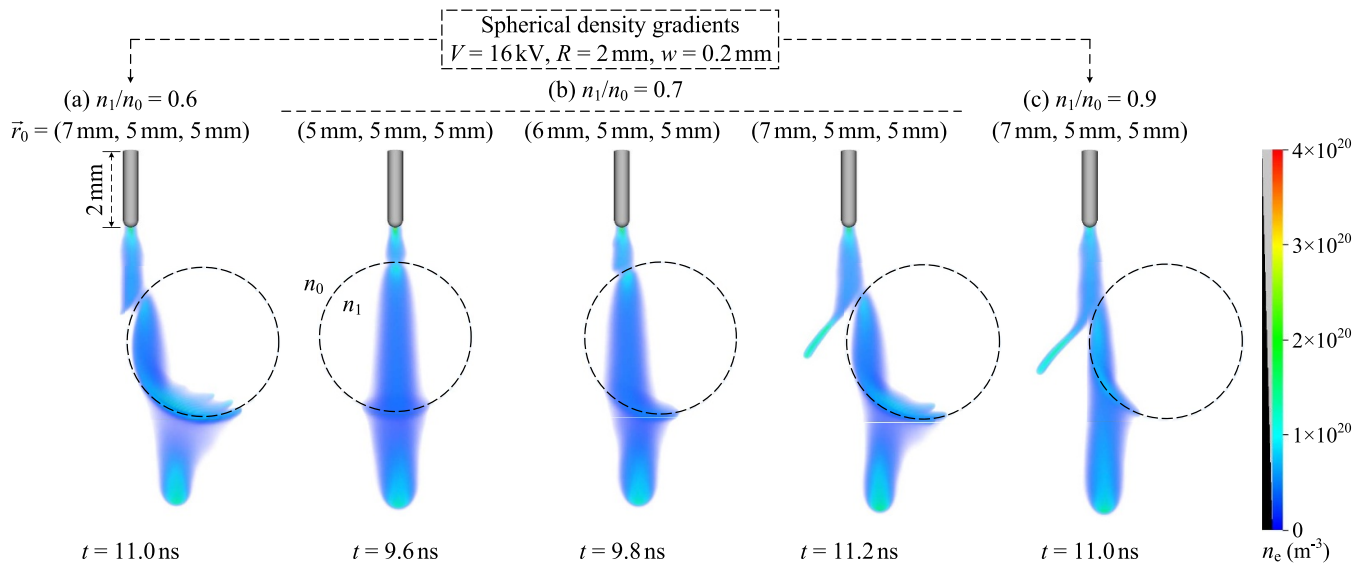


Figure 11. The interaction between a streamer and a spherical density gradient for $n_1/n_0 < 1$. Panels (a) and (c) show streamers for different density ratios n_1/n_0 at a gradient center $\vec{r}_0 = (7 \text{ mm}, 5 \text{ mm}, 5 \text{ mm})$, whereas panel (b) shows streamers for different gradient centers \vec{r}_0 at a density ratio $n_1/n_0 = 0.7$.

along the surface. In addition, increasing the density ratio to $n_1/n_0 = 0.9$ results in less discharge growth inside the sphere, see figure 11(c).

4.2. Hemispherical density gradient

We now look into the interaction between a positive streamer and a hemispherical density gradient, see figure 2(d) and table 2. The effect of the air density ratio n_1/n_0 on streamer propagation from a low-density region to a high-density region is illustrated in figure 12. The simulations are performed at an

applied voltage $V = 16 \text{ kV}$ with a gradient center $\vec{r}_0 = (5 \text{ mm}, 5 \text{ mm}, 10 \text{ mm})$, a radius $R = 5 \text{ mm}$ and a width $w = 0.2 \text{ mm}$.

Figure 12(a) shows that for $n_1/n_0 = 1.2$ the streamer can propagate through the gradient and continue its propagation with two small branches. When the density ratio increases to $n_1/n_0 = 1.4$, the streamer splits into several branches when it encounters the gradient, see figure 12(b). Increasing n_1/n_0 to fall between 1.6 and 1.8 causes the streamer to split into two parts upon encountering the gradient, where the first part penetrates into the high-density region with multiple branching channels, and the second part propagates sideways along the

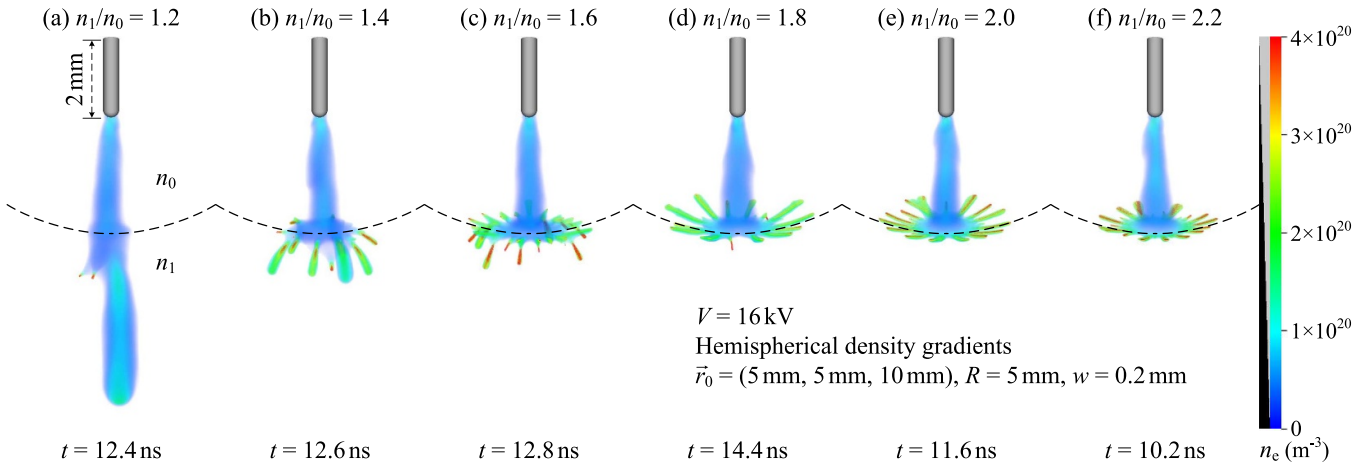


Figure 12. Interaction with a hemispherical density gradient for different density ratios n_1/n_0 . The hemispherical gradient is partly indicated by a dashed curve.

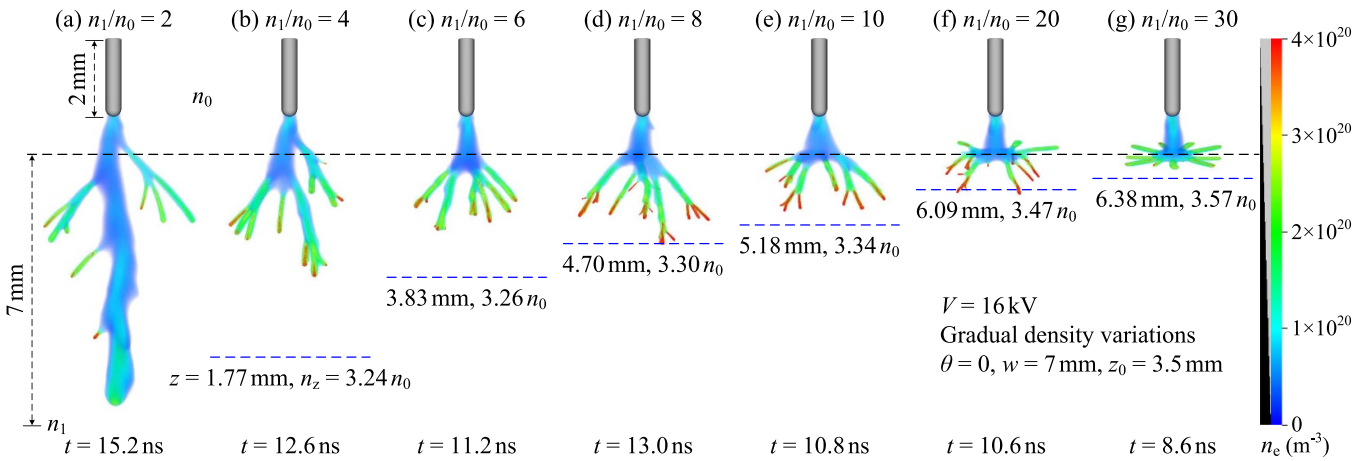


Figure 13. Interaction with gradual density variations for different density ratios n_1/n_0 . The gas density linearly increases between the black dashed line and the bottom of the figure, over a width $w = 7$ mm. For reference, the locations at which the reduced background electric field E_{bg}/n is equal to the approximate reduced stability field E_{st}/n_0 are indicated by blue dashed lines, using $E_{st} = 5 \text{ kV cm}^{-1}$ [64]. The height z and the actual gas density n_z for these blue lines are also given.

surface, see figures 12(c) and (d). Finally, when n_1/n_0 exceeds 2.0, the streamer only propagates sideways along the surface with multiple branching channels, forming a flower-like structure, see figures 12(e) and (f). These channels slightly bend upwards, which is surprising since the background electric field is directed downwards. Note that the sideward discharge shows high electron densities in the branching channels, and it decelerates and tends to stagnate.

We find that the ability of a gradient to inhibit streamer propagation depends not only on its angle but also on its shape. This is demonstrated in figures 3, 10 and 12, where we observe that with the same parameters of $V = 16 \text{ kV}$, $w = 0.2 \text{ mm}$ and $\theta = 0$, a convex spherical gradient is the most effective in inhibiting streamer propagation ($n_1/n_0 \geq 1.4$), followed by a planar gradient ($n_1/n_0 \geq 1.8$) and a concave hemispherical gradient ($n_1/n_0 \geq 2.0$).

4.3. Gradual density variation

Finally, we study how a positive streamer interacts with a much wider density gradient, using $w = 7 \text{ mm}$, see figure 2(b) and table 2. The effect of the air density ratio n_1/n_0 is illustrated in figure 13. The simulations are performed at an applied voltage $V = 16 \text{ kV}$. We note that they are somewhat unrealistic, as they do not take into account the variation of the photon absorption length with the gas density, which is left for future work.

Figure 13(a) shows that for $n_1/n_0 = 2$ the streamer can penetrate into the gradient accompanied by the formation of several side branches. As the density ratio increases, more branching channels form with smaller diameters and higher electron densities at their tips, see figures 13(b)–(f). Branching angles increase as well, since it is more difficult for the discharge to propagate downwards inside the gradient.

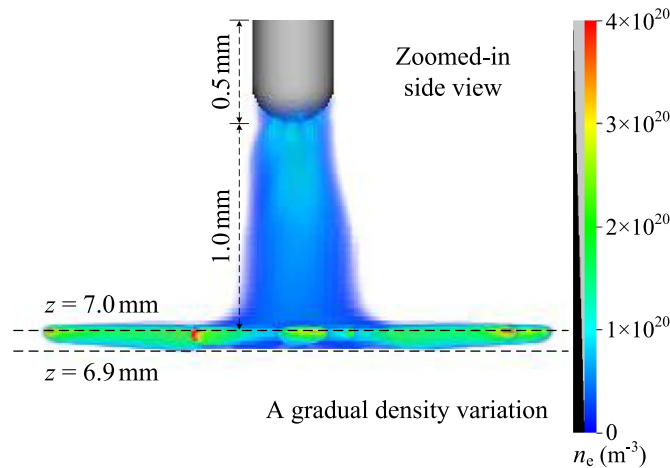


Figure 14. Zoomed-in side view of figure 13(g) with $n_1/n_0 = 30$. The streamer only slightly penetrates into the gradient, over a vertical distance of less than 0.1 mm. Similar behavior was found for other cases in which streamers did not propagate into the high-density region.

When the density ratio increases to $n_1/n_0 = 30$, the streamer is no longer able to penetrate into the gradient but propagates along the surface, see figures 13(g) and 14. We remark that for the other cases streamer propagation is expected to stop after some distance, when the reduced background electric field E_{bg}/n becomes too low. For reference, the locations where E_{bg}/n equals the approximate reduced streamer stability field E_{st}/n_0 are indicated in figure 13.

5. Discussion

5.1. The threshold for inhibiting streamer propagation

We have shown that the density ratio threshold for inhibiting streamer propagation from a low-density region to a high-density region depends on the gas gradient width, the type of gradient, the gradient angle and the applied voltage. To further investigate this threshold, we focus on a planar gradient with a center height $z_0 = 5$ mm and an angle $\theta = 0$. At $V = 16$ kV, we approximately determine the density ratio n_1/n_0 required to inhibit streamer propagation for various gradient widths, as illustrated in figure 15. For $w = 0.1$ mm, $w = 0.2$ mm and $w = 0.4$ mm, we find that the required density ratios are about 1.35, 1.7 and 2.4, respectively.

The above values all correspond to a similar density slope, given by

$$(n_1 - n_0)/w \approx 3.5 n_0/\text{mm}, \quad (3)$$

which furthermore agrees rather well with the slope obtained from figure 13(g), which is about $4n_0/\text{mm}$. This can be explained by considering the reduced background electric field E/n ahead of the streamer. Normally, a streamer grows in the forward direction, since E/n is highest there. However, when the density slope exceeds a certain threshold, sideward growth is stronger than forward growth (due to the increasing density in the forward direction), which deforms the streamer and leads to propagation along the surface.

We remark that the above density slope for inhibiting streamer propagation is not unique; it depends on many factors, including the gradient geometry (e.g. its angle) and the primary streamer properties (e.g. the radius), which can be affected by changing the applied voltage and the gas density n_0 . Furthermore, the gradient width should be comparable to the streamer radius or larger.

5.2. Effect of inhomogeneous gas composition

In the present study the gas density was spatially varied, leading to a variation in E/n that affected electron transport and reaction coefficients, but the gas composition was always 20% O_2 and 80% N_2 . In some plasma devices, such as plasma jets, there is instead a spatial variation in the gas composition, see e.g. [65–67]. In the different gases, electron transport and reaction coefficients will also differ. Depending on the particular gases used, such a variation could lead to similar effects as observed in this paper. However, some of the discharge dynamics can be rather different in such inhomogeneous mixtures, for example due to Penning ionization or due to significant differences in photoionization between the gases.

5.3. Gas density effect on photoionization

We have not taken the effect of the gas density on the photon absorption length into account when computing photoionization. These absorption lengths scale like $1/n$ [45]. When a positive streamer propagates from a low gas density to a high gas density, this will result in a higher photoionization density at the boundary of the high-density region. How strong this effect will be depends on the gas density ratio and the width of the gradient, where it should be noted that typical photon absorption distances are rather small (less than a mm in air at 1 bar). For sharp gradients and large density ratios, the locally increased photoionization density could further enhance the surface propagation mode, thereby also increasing the ‘diode effect’ discussed in [13].

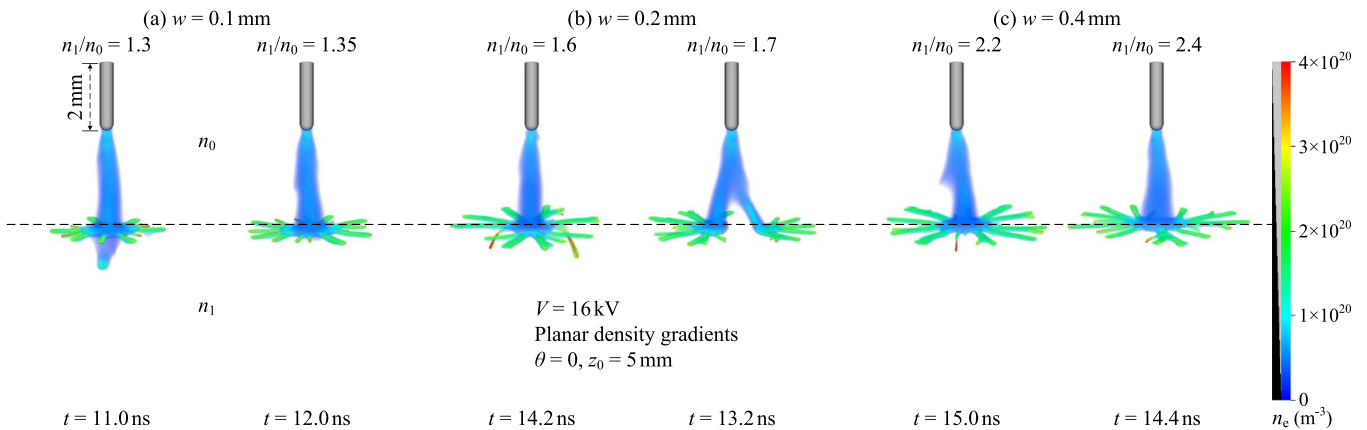


Figure 15. The density ratio n_1/n_0 required to inhibit streamer propagation through a planar density gradient for three different gradient widths w .

For most cases presented in this paper, the gas density ratio was below a factor of two. Based on past simulation work [49], we do not expect major differences in streamer properties like radius or velocity if gas-dependent photon absorption lengths were taken into account. However, it was recently shown that streamer branching can be quite sensitive to the amount of photoionization [50]. We leave the exploration of these effects for future work.

6. Conclusions

We have studied the effect of gas density inhomogeneities on positive streamer discharges in air using a 3D fluid model, generalizing the 2D axisymmetric fluid simulations of [13]. In order to realistically simulate streamer branching, we included a stochastic photoionization model with discrete photons. Various types of planar and (hemi)spherical gas density gradients were considered. Streamers propagated from a region of density n_0 towards a region of higher or lower gas density n_1 , where n_0 corresponds to 300 K and 1 bar. Streamers could always propagate into a region with a lower gas density and their paths deviated towards nearby low-density regions. For the case of low-to-high gas density, we observed streamer branching at the density gradient, with branches growing in a flower-like pattern over the gradient surface. Depending on the gas density ratio, the gradient width and other factors, narrow branches were able to propagate into the higher-density gas. In a planar geometry, we found such propagation was possible up to a gas density slope of $3.5n_0/\text{mm}$. This value was dependent on a number of conditions, such as the gradient angle. Surprisingly, a higher applied voltage made it more difficult for streamers to penetrate into the high-density region, due to an increase of the primary streamer's radius.

Data availability statement

The data that support the findings of this study are openly available at the following URL/DOI: <https://doi.org/10.5281/zenodo.7927427>.

Acknowledgment

B G was funded by the China Scholarship Council (CSC) (Grant No. 201906280436).

Appendix. Implementation of gas density variation

Below, we explain how the gas density variations were implemented in the code. For the planar density gradients and gradual density variations, we first define a plane from coefficients (a, b, c, d) as

$$ax + by + cz + d = 0. \quad (\text{A.1})$$

For every grid cell in the domain, the signed distance $f(x, y, z)$ to this surface is computed as

$$f(x, y, z) = \frac{ax + by + cz + d}{\sqrt{a^2 + b^2 + c^2}}. \quad (\text{A.2})$$

For $f(x, y, z) < -w/2$, where w is the width of the gradient, the gas density n is given by $n = n_0$. For $f(x, y, z) > w/2$ it is $n = n_1$, and for values in between the density is linearly interpolated between n_0 and n_1 . When the mesh is refined, the gas density is recomputed on the finer grid.

Spherical and hemispherical density gradients are defined by coordinates $\vec{r}_0 = (x_0, y_0, z_0)$ and a radius R . The signed distance to the sphere is then determined in every grid cell as

$$f(x, y, z) = \sqrt{(x - x_0)^2 + (y - y_0)^2 + (z - z_0)^2} - R. \quad (\text{A.3})$$

For spherical gradients, we then have $n = n_1$ for $f(x, y, z) < -w/2$ and $n = n_0$ for $f(x, y, z) > w/2$, with densities linearly interpolated in between. The same is used for hemispherical gradients, but n_0 and n_1 are swapped, so that the density inside the hemisphere is always n_0 .

ORCID iDs

Baohong Guo  <https://orcid.org/0000-0001-8368-5014>
 Ute Ebert  <https://orcid.org/0000-0003-3891-6869>
 Jannis Teunissen  <https://orcid.org/0000-0003-0811-5091>

References

- [1] Nijdam S, Teunissen J and Ebert U 2020 The physics of streamer discharge phenomena *Plasma Sources Sci. Technol.* **29** 103001
- [2] Zhao Z, Li C, Zheng X, Sun A and Jiangtao Li 2022 Periodical discharge regime transitions under long-term repetitive nanosecond pulses *Plasma Sources Sci. Technol.* **31** 045005
- [3] Hare B M *et al* 2019 Needle-like structures discovered on positively charged lightning branches *Nature* **568** 360–3
- [4] Stenbaek-Nielsen H C, Kanmae T, McHarg M G and Haaland R 2013 High-speed observations of sprite streamers *Surv. Geophys.* **34** 769–95
- [5] Seeger M, Avaheden J, Pancheshnyi S and Votteler T 2017 Streamer parameters and breakdown in CO₂ *J. Phys. D: Appl. Phys.* **50** 015207
- [6] Seeger M, Votteler T, Ekeberg J, Pancheshnyi S and Sánchez L 2018 Streamer and leader breakdown in air at atmospheric pressure in strongly non-uniform fields in gaps less than one metre *IEEE Trans. Dielectr. Electr. Insul.* **25** 2147–56
- [7] Wang D and Namihira T 2020 Nanosecond pulsed streamer discharges: II. Physics, discharge characterization and plasma processing *Plasma Sources Sci. Technol.* **29** 023001
- [8] Adamovich I *et al* 2022 The 2022 plasma roadmap: low temperature plasma science and technology *J. Phys. D: Appl. Phys.* **55** 373001
- [9] Briels T M P, van Veldhuizen E M and Ebert U 2008 Positive streamers in air and nitrogen of varying density: experiments on similarity laws *J. Phys. D: Appl. Phys.* **41** 234008
- [10] Ebert U, Nijdam S, Chao Li, Luque A, Briels T and van Veldhuizen E 2010 Review of recent results on streamer discharges and discussion of their relevance for sprites and lightning *J. Geophys. Res. Space Phys.* **115** A00E43
- [11] Pasko V P, Inan U S and Bell T F 1998 Spatial structure of sprites *Geophys. Res. Lett.* **25** 2123–6
- [12] Kosarev I N, Yu Starikovskiy A and Aleksandrov N L 2019 Development of high-voltage nanosecond discharge in strongly non-uniform gas *Plasma Sources Sci. Technol.* **28** 015005
- [13] Yu Starikovskiy A and Aleksandrov N L 2019 ‘Gas-dynamic diode’: streamer interaction with sharp density gradients *Plasma Sources Sci. Technol.* **28** 095022
- [14] Yu Starikovskiy A and Aleksandrov N L 2020 Blocking streamer development by plane gaseous layers of various densities *Plasma Sources Sci. Technol.* **29** 034002
- [15] Marode E, Bastien F and Bakker M 1979 A model of the streamer-induced spark formation based on neutral dynamics *J. Appl. Phys.* **50** 140–6
- [16] Kacem S, Ducasse O, Eichwald O, Yousfi M, Meziane M, Philippe Sarrette J P and Charrada K 2013 Simulation of expansion of thermal shock and pressure waves induced by a streamer dynamics in positive DC corona discharges *IEEE Trans. Plasma Sci.* **41** 942–7
- [17] Komuro A and Ando A 2017 Effect of voltage amplitude on gas density variation in an atmospheric pressure streamer discharge *Eur. Phys. J. Appl. Phys.* **78** 20802
- [18] Peng B, Jiang N, Shang K, Lu N, Jie Li and Yan W 2022 Characteristics of three-electrode pulsed surface dielectric barrier discharge: streamer-to-spark transition and hydrodynamic expansion *J. Phys. D: Appl. Phys.* **55** 265202
- [19] Ono R and Oda T 2004 Visualization of streamer channels and shock waves generated by positive pulsed corona discharge using laser schlieren method *Jpn. J. Appl. Phys.* **43** 321–7
- [20] Ono R, Teramoto Y and Oda T 2010 Gas density in a pulsed positive streamer measured using laser shadowgraph *J. Phys. D: Appl. Phys.* **43** 345203
- [21] Liu Q and Zhang Y 2014 Shock wave generated by high-energy electric spark discharge *J. Appl. Phys.* **116** 153302
- [22] Ono R 2018 Rapid temperature increase near the anode and cathode in the afterglow of a pulsed positive streamer discharge *J. Phys. D: Appl. Phys.* **51** 245202
- [23] Cui Y, Zhuang C, Zeng R and Zhou X 2019 Shock wave in a long-air-gap leader discharge *AIP Adv.* **9** 065011
- [24] Komuro A, Tsukada H and Ando A 2019 Slow gas heating process in an atmospheric-pressure streamer discharge visualized by high-speed schlieren method *IEEE Trans. Plasma Sci.* **47** 1164–71
- [25] Komuro A, Natsume C and Ando A 2021 Measurement of gas-density variation in pulsed streamer discharge at atmospheric pressure by Mach–Zehnder interferometry *Plasma Sources Sci. Technol.* **30** 095007
- [26] Köhn C, Chanrion O and Neubert T 2018 High-energy emissions induced by air density fluctuations of discharges *Geophys. Res. Lett.* **45** 5194–203
- [27] Köhn C, Chanrion O, Babich L P and Neubert T 2018 Streamer properties and associated x-rays in perturbed air *Plasma Sources Sci. Technol.* **27** 015017
- [28] Köhn C, Chanrion O, Nishikawa K, Babich L and Neubert T 2020 The emission of energetic electrons from the complex streamer corona adjacent to leader stepping *Plasma Sources Sci. Technol.* **29** 035023
- [29] Grachev L P, Esakov I I and Khodataev K V 1999 Microwave streamer discharge in a supersonic air flow *Tech. Phys.* **44** 1271–5
- [30] Fleming E L, Jackman C H, Considine D B and Stolarski R S 2001 Sensitivity of tracers and a stratospheric aircraft perturbation to two-dimensional model transport variations *J. Geophys. Res. Atmos.* **106** 14245–63
- [31] Gumbel J 2001 Aerodynamic influences on atmospheric in situ measurements from sounding rockets *J. Geophys. Res. Space Phys.* **106** 10553–63
- [32] Lawson S J and Barakos G N 2011 Review of numerical simulations for high-speed, turbulent cavity flows *Prog. Aerosp. Sci.* **47** 186–216
- [33] Niknezhad M, Chanrion O, Köhn C, Holbøll J and Neubert T 2021 A three-dimensional model of streamer discharges in unsteady airflow *Plasma Sources Sci. Technol.* **30** 045012
- [34] Bletzinger P, Ganguly B N, Van Wie D and Garscadden A 2005 Plasmas in high speed aerodynamics *J. Phys. D: Appl. Phys.* **38** R33–R57
- [35] Yu Starikovskii A, Nikipelov A A, Nudnova M M and Roupasov D V 2009 SDBD plasma actuator with nanosecond pulse-periodic discharge *Plasma Sources Sci. Technol.* **18** 034015
- [36] Leonov S B, Adamovich I V and Soloviev V R 2016 Dynamics of near-surface electric discharges and mechanisms of their interaction with the airflow *Plasma Sources Sci. Technol.* **25** 063001
- [37] Zhang C, Huang B, Luo Z, Che X, Yan P and Shao T 2019 Atmospheric-pressure pulsed plasma actuators for flow control: Shock wave and vortex characteristics *Plasma Sources Sci. Technol.* **28** 064001
- [38] Longfei Li and Wang J 2022 Nanosecond dielectric barrier discharge on a curved surface in atmospheric air: streamer evolution and aerodynamic perturbations *J. Phys. D: Appl. Phys.* **55** 055203
- [39] Guerra-García C, Martínez-Sánchez M, Miles R B and Starikovskiy A 2015 Localized pulsed nanosecond

- discharges in a counterflow nonpremixed flame environment *Plasma Sources Sci. Technol.* **24** 055010
- [40] Luque A and Ebert U 2009 Emergence of sprite streamers from screening-ionization waves in the lower ionosphere *Nat. Geosci.* **2** 757–60
- [41] Luque A and Ebert U 2010 Sprites in varying air density: charge conservation, glowing negative trails and changing velocity *Geophys. Res. Lett.* **37** L06806
- [42] Qin J and Victor P P 2015 Dynamics of sprite streamers in varying air density *Geophys. Res. Lett.* **42** 2031–6
- [43] Opaits D F, Shneider M N, Howard P J, Miles R B and Milikh G M 2010 Study of streamers in gradient density air: table top modeling of red sprites *Geophys. Res. Lett.* **37** L14801
- [44] Teunissen J and Ebert U 2017 Simulating streamer discharges in 3D with the parallel adaptive Afivo framework *J. Phys. D: Appl. Phys.* **50** 474001
- [45] Zheleznyak M B, Mnatsakanyan A K and Sizykh S V 1982 Photo-ionization of nitrogen and oxygen mixtures by radiation from a gas-discharge *High Temp.* **20** 357–62
- [46] Luque A, Ebert U, Montijn C and Hundsdoerfer W 2007 Photoionization in negative streamers: fast computations and two propagation modes *Appl. Phys. Lett.* **90** 081501
- [47] Bourdon A, Pasko V P, Liu N Y, Célestin S, Ségur P and Marode E 2007 Efficient models for photoionization produced by non-thermal gas discharges in air based on radiative transfer and the Helmholtz equations *Plasma Sources Sci. Technol.* **16** 656–78
- [48] Chanrion O and Neubert T 2008 A PIC-MCC code for simulation of streamer propagation in air *J. Comput. Phys.* **227** 7222–45
- [49] Bagheri B and Teunissen J 2019 The effect of the stochasticity of photoionization on 3D streamer simulations *Plasma Sources Sci. Technol.* **28** 045013
- [50] Wang Z, Dijcks S, Guo Y, Van Der Leege M, Sun A, Ebert U, Nijdam S and Teunissen J 2023 Quantitative modeling of streamer discharge branching in air *Plasma Sources Sci. Technol.* **32** 085007
- [51] Teunissen J and Ebert U 2018 Afivo: a framework for quadtree/octree AMR with shared-memory parallelization and geometric multigrid methods *Comput. Phys. Commun.* **233** 156–66
- [52] Teunissen J and Schiavello F 2023 Geometric multigrid method for solving Poisson's equation on octree grids with irregular boundaries *Comput. Phys. Commun.* **286** 108665
- [53] Hagelaar G J M and Pitchford L C 2005 Solving the Boltzmann equation to obtain electron transport coefficients and rate coefficients for fluid models *Plasma Sources Sci. Technol.* **14** 722–33
- [54] Phelps database (N₂, O₂) (available at: www.lxcat.net) (Accessed 6 January 2023)
- [55] Phelps A V and Pitchford L C 1985 Anisotropic scattering of electrons by N₂ and its effect on electron transport *Phys. Rev. A* **31** 2932–49
- [56] Lawton S A and Phelps A V 1978 Excitation of the $b^1\Sigma_g^+$ state of O₂ by low energy electrons *J. Chem. Phys.* **69** 1055
- [57] Pancheshnyi S 2013 Effective ionization rate in nitrogen–oxygen mixtures *J. Phys. D: Appl. Phys.* **46** 155201
- [58] Kossyi I A, Yu Kostinsky A, Matveyev A A and Silakov V P 1992 Kinetic scheme of the non-equilibrium discharge in nitrogen–oxygen mixtures *Plasma Sources Sci. Technol.* **1** 207–20
- [59] Aleksandrov N L and Bazelyan E M 1999 Ionization processes in spark discharge plasmas *Plasma Sources Sci. Technol.* **8** 285–94
- [60] Nijdam S, van de Wetering F M J H, Blanc R, van Veldhuizen E M and Ebert U 2010 Probing photo-ionization: experiments on positive streamers in pure gases and mixtures *J. Phys. D: Appl. Phys.* **43** 145204
- [61] Guo B, Xiaoran Li, Ebert U and Teunissen J 2022 A computational study of accelerating, steady and fading negative streamers in ambient air *Plasma Sources Sci. Technol.* **31** 095011
- [62] Teunissen J 2020 Improvements for drift-diffusion plasma fluid models with explicit time integration *Plasma Sources Sci. Technol.* **29** 015010
- [63] Childs H *et al* 2012 VisIt: an end-user tool for visualizing and analyzing very large data *High Performance Visualization—Enabling Extreme-Scale Scientific Insight* (Chapman and Hall/CRC) pp 357–72
- [64] Allen N L and Boutlondj M 1991 Study of the electric fields required for streamer propagation in humid air *IEE Proc. A* **138** 37
- [65] Naidis G V 2011 Modelling of plasma bullet propagation along a helium jet in ambient air *J. Phys. D: Appl. Phys.* **44** 215203
- [66] Xiong R, Xiong Q, Anton Y, Nikiforov P V and Leys C 2012 Influence of helium mole fraction distribution on the properties of cold atmospheric pressure helium plasma jets *J. Appl. Phys.* **112** 033305
- [67] Boeuf J-P, Yang L L and Pitchford L C 2013 Dynamics of a guided streamer ('plasma bullet') in a helium jet in air at atmospheric pressure *J. Phys. D: Appl. Phys.* **46** 015201